Super-resolution electron ptychography of low dimensional materials at 30keV beyond the detector limit

C.S. Allen[1,2,a)], M. Danaie[2], J. Warner[3,4], D. J. Batey[5] and A. I. Kirkland[1,2,6]

1. Department of Materials, University of Oxford, Oxford, UK. OX1 3PH

2. Electron Physical Science Imaging Centre, Diamond Light Source Ltd, Didcot, UK. OX11 0DE, UK

3. Materials Science and Engineering Program, Texas Materials Institute, The University of Texas at Austin, Austin, Texas, US

4. Walker Department of Mechanical Engineering, The University of Texas at Austin, Austin, Texas, US

5. Diamond Light Source Ltd, Didcot, UK. OX11 0DE

6. Rosalind Franklin Institute, Harwell Campus, Didcot, UK. OX11 0QX

a) Author to whom correspondence should be addressed: christopher.allen@materials.ox.ac.uk

Abstract

We demonstrate that electron ptychographic phase reconstruction can recover spatial frequencies higher than those directly recorded in the experimental electron diffraction patterns. This ability to recover high angle information from the oversampled low angle information allows an annular detector to be inserted which partially shadows a lower pixelated detector to simultaneously record a conventional annular dark field image and a ptychographic data set. We apply this approach to 30keV imaging of monolayer molybdenum disulfide and achieve an Abbe limited resolution of 1.2 ± 0.1Å in our reconstructions.

Transmission electron microscopy (TEM) is a key tool for the characterisation of materials and aberration-corrected instruments routinely achieve sub-Ångstrom resolution [1]. TEMs typically operate at electron energies between 80 and 300keV and, as the effect of optical aberrations scale as a power law with wavelength, higher resolutions are achieved at higher electron energy [2]. However, for light element materials momentum transfer from the incident electron beam can break atomic bonds and destroy the crystal structure [3]. One approach to mitigating this is to operate at lower accelerating voltages and specialist instruments have been developed which combine spherical aberration correction with a monochromatic electron source and / or chromatic aberration correctors. These instruments have demonstrated Ångstrom level resolution at electron energies of 30keV and lower [4–6]. However atomic resolution imaging at 30keV remains beyond the reach of the majority of third order spherical aberration corrected electron microscopes.

Recent advances in detector technology [7] have been the catalyst for developments in electron diffractive imaging methods [8] and ptychographic reconstructions have been demonstrated at resolutions limited only by atomic vibrations in the sample [9]. Importantly, the resolution in a ptychographic reconstruction is decoupled from the optical system of the microscope, relaxing the requirements for complex electron optical aberration correction elements. However, the application of electron ptychography at low voltages has been limited, with only an initial demonstration at 30keV within an SEM obtaining a resolution of 2.4Å [10,11].

Electron ptychography is a dose efficient imaging mode [12–14] and is thus ideally suited to structural studies of beam sensitive materials. Ptychography quantitatively recovers the relative phase change of the electron wave through the sample and is not limited by the weak phase approximation [15,16]. Furthermore it is possible to recover information about the measured object at spatial frequencies beyond those directly recorded in the diffraction pattern via iterative methods originally proposed by Gerchberg for coherent diffractive imaging [17] and subsequently implemented for super-resolution optical ptychography by Maiden et al. [18]

Here we demonstrate at least 1.2Å resolution ptychographic phase retrieval of two-dimensional molybdenum disulphide (MoS_2) at an incident beam energy of 30keV in a JEOL ARM300CF third-order aberration corrected TEM. Importantly this instrument does not have monochromated optics, chromatic aberration correction or fifth order aberration correction [19] as has been previously required for atomic resolution imaging at 30keV [20]. In an alternative approach we achieve atomic resolution by using the power of ptychography to achieve a resolution beyond the 2α limit, where α is the illumination convergence semi-angle. We exploit the super-resolution capability of ptychography to recover information at higher frequencies than those directly measured in the diffraction pattern by allowing the iterative algorithm to freely update regions beyond the edges of the detector. [18] This enables us to collect a medium-angle annular dark field (MAADF) signal using a fast monolithic detector simultaneously with the four-dimensional scanning electron diffraction dataset required for ptychographic reconstruction.

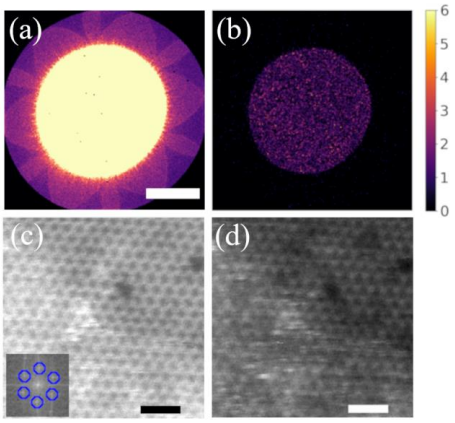

Figure 1. (a) Position averaged convergent beam electron diffraction pattern, scale bar represents 20 mrad. (b) Example individual diffraction pattern with color bar showing the number of counts recorded. (c) Simultaneously recorded MAADF image (inset: calculated power spectrum with 2.73 Å reflections marked). (d) LAADF image reconstructed from the 4D data set. Scale bars represent 1 nm.

A four-dimensional STEM (4DSTEM) dataset consists of two-dimensional far-field (Fraunhofer) diffraction patterns recorded at each location in a two-dimensional array of probe positions. Ptychography relies on oversampling in the four-dimensional data set to recover the complex exit wave-function and to decouple the electron illumination from the complex transmission function

of the object being imaged [21]. This is done using either an iterative algorithm such as the extended ptychographical iterative engine or ePIE [22] or by direct methods [23].

Due to a Fourier relationship between the image and diffraction planes, the real-space pixel size of an ePIE reconstruction is determined by the maximum scattering angle in the measured diffraction pattern, with larger scattering angle corresponding to a smaller real space pixel. The resolution in the reconstruction is therefore constrained by the maximum scattering angle collected in the diffraction pattern unless super-resolution reconstruction techniques are used.

Due to the longer electron wavelength at low incident beam energy, equivalent spatial frequencies are recorded at higher angles. However, the maximum possible scattering angle recorded on the detector can be limited by fixed apertures or, in a double corrected TEM, by residual aberrations in the image-side corrector. Furthermore, due to finite dynamic range of the detector it is often desirable to work at a long camera length to spread the relatively high intensity bright field disc (BFD) across many pixels to avoid saturation. This is particularly true when operating detectors at low bit depth in order to maximize data acquisition speed [24].

The resolution of a ptychographic reconstruction is ultimately limited by electron dose. At a fixed electron dose there will be a scattering angle above which the number of scattered electrons is insufficient for any recoverable information at that frequency. It is therefore desirable to collect data at a camera length for which there is little intensity on pixels at the edge of the detector resulting in the resolution of the reconstruction being effectively dose limited. Other collection geometries result in electrons which could be used to increase the resolution of the reconstruction not being measured. At low electron energies this is not always possible due to detector saturation and the presence of fixed apertures. Consequently, when using a large convergence semi-angle, significant electron intensity is recorded at the edge of the detector and these electrons have interfered with the sample at spatial frequencies above those directly related to the maximum detector collection angle. In the reconstruction process, these higher frequencies need to be considered.

Experimental data was recorded at an accelerating voltage of 30keV on a JEOL ARM300CF double corrected electron microscope. Data was recorded on a MerlinEM Medipix3 detector which has excellent response characteristics for low voltage electrons [25,26]. A monolayer MoS_2 sample was chosen as a test specimen for this study and was heated to 400°C using a DENS wildfire in-situ heating holder to minimize surface contamination. A 4DSTEM data set was recorded by scanning a focused electron probe relative to the sample on a 256 x 256 grid, with a step size of approximately 0.2Å. The exposure time for each diffraction pattern was 1ms.

The microscope was aligned with an illumination convergence semi-angle, α, of 26mrad with a beam current of 12pA. At 30keV, the chromatic aberration coefficient of the JEOL ARM300CF microscope is estimated to be C_c = 0.76mm and energy spread of the source dE=0.45eV. The spherical aberration co-efficient was tuned to approximately C_s = 7um. Under these conditions the probe is largely aberration free out to 26mrad and the diffraction limited resolution of the microscope is $r_d = \frac{0.61\lambda}{\alpha} = 1.6$Å with λ the electron wavelength. Chromatic aberration introduces an effective focal spread to the beam approximately equal to $\delta_C = C_C \left(\frac{dE}{E}\right)$, [27] and increases the FWHM of the probe from 1.4Å to 1.72Å (see Supplementary Figure S1). It has been shown that ptychographic imaging is somewhat robust to the effect of chromatic blur as defocus causes a symmetric phase shift to the incident beam which is also present in diffracted beams and therefore

does not change the interference pattern at the center of the overlap region. [28] Furthermore, a finite electron energy spread will introduce an effective point spread function to the diffraction pattern as there will be a range of scattering angles for each reflection due to the range of wavelengths in the illumination. For dE=0.45eV the maximum wavelength spread is $d\lambda = \pm\ 5.4 \times 10^{-17}\ m$. For the maximum scattering angle recorded in this experiment (41mrad) this wavelength spread would result in a change of scattering vector of 6.3×10^{-4}mrad. For these experiments, the pixel size in the detector is equal to 0.3mrad, over two orders of magnitude larger than the blur due to chromatic spread and therefore can be effectively ignored. For a larger energy spreads, techniques have been developed to include the incoherent sum of multiple energies in the reconstruction algorithm. [29,30]

A position averaged convergent beam electron diffraction pattern (PACBED) is shown in Figure 1a. Figure 1b shows a single diffraction pattern recorded with a 1ms exposure time. The cutoff at higher angles evident in Figure 1a is due to the presence of an additional annular dark field (ADF) detector with an inner collection angle of 41mrad. Due to the weak high angle scattering from low dimensional materials, a relatively low inner collection angle is typically used to record high contrast ADF images. The presence of the ADF detector enables the simultaneous acquisition of a MAADF image (Figure 1c) with significantly higher contrast that the virtual low angle annular dark field (LAADF) image reconstructed from the 4D dataset (Figure 1d). The power spectrum of the ADF image shows the 2.7Å reflections of the MoS_2 lattice (Figure 1c, inset).

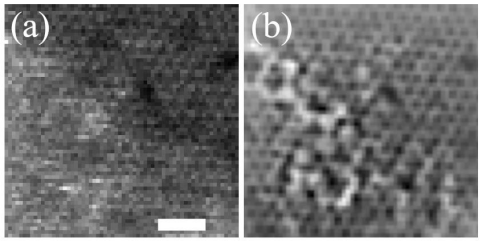

Figure 2. (a) LAADF image reconstructed from a subset of recorded diffraction patterns used for the ePIE reconstruction. (b) Phase of the object reconstructed using ePIE. The scale bar represents 1nm.

All ptychographic reconstructions were performed using the ePIE operator in PtyRex [31] on a subset of the recorded 4D data with scan position annealing to correct for small variations in the probe positions [32], 16 probe modes to account for partial spatial coherence in the electron source [33,34] (Supplementary Figure S2), and 1000 iterations.

Figure 2a shows a virtual LAADF image reconstructed using one sixteenth of the probe positions in the full data set (one in four probe positions in both x and y directions). A subset of the data was used as the illumination probe was sufficiently large (3Å full width at $1/e^2$ intensity) to provide a real space probe overlap of 74%, sufficient for ptychographic reconstruction (see Supplementary Figure S3). The effective electron dose for the ptychographic reconstruction was approximately 120,000eÅ^{-2}. The phase of the reconstructed object function is shown in Figure 2b. A 17.5cm camera length was used with a maximum collection semi-angle of 41mrad. At 30keV this

corresponds to a reconstruction pixel size of 0.85Å, a diagonal pixel to pixel distance of 1.2Å and maximum Nyquist limit of 2.4Å precluding the possibility of fully resolving the splitting between the Mo and 2S sites (Figure 3 f-h).

The lower left portion of the sample shown in Figure 2a is covered with an amorphous surface contaminant common in low dimensional materials. In the LAADF image, in which the contributions to image intensity are predominantly incoherent, this contaminant largely obscures the periodic structure of the underlying MoS_2. In the coherent ptychographic phase image (Figure 2b) the underlying MoS_2 structure is partially visible, and the intensity is due to the cumulative phase shift of the electrons as they pass through both the amorphous surface contaminant and crystalline MoS_2 sample. In these regions the intensity in the phase image cannot be directly interpreted as atomic structure and detailed comparison with simulation for accurate interpretation.

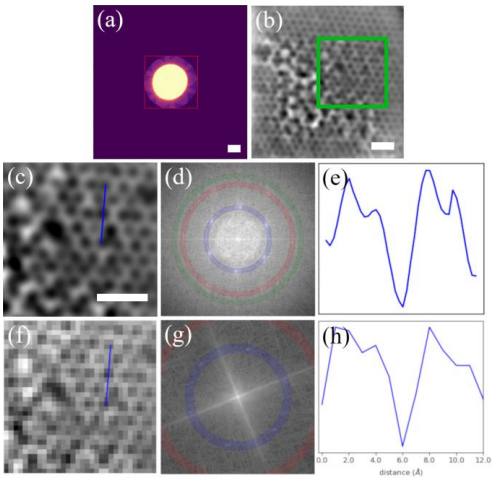

Figure 3. (a) PACBED pattern after zero padding to 3 times the detector collection angle (the detector area is marked in red), scale bar represents 20mrad. (b) Object phase reconstructed using the zero-padded data, scale bar represents 1nm. (c) Zoomed image from the region marked with the green box in (b), scale bar represents 1nm. (d) Power spectrum calculated from (b). The blue, red and green rings represent the 2.73Å $\langle 10\bar{1}0\rangle$, 1.58Å $\langle 11\bar{2}0\rangle$ and 1.36Å $\langle 1\bar{2}00\rangle$ MoS_2 reflections respectively. (e) Intensity line scan taken from the position marked with the blue line in (c). (f) Zoomed image, (g) power spectrum and (h) line scan taken from the corresponding area in the non-padded reconstruction in Figure 2b.

One approach to decrease the pixel size in a ptychographic reconstructions is to pad the input diffraction patterns with zeros [11] without allowing the algorithm to add information to the zero-padded regions. This decreases the pixel dimensions in the real-space reconstructed image. Figure 3b shows the reconstructed phase using diffraction patterns zero-padded to a semi-angle of

123mrad giving a corresponding pixel size in the reconstructed image of 0.29Å. Visual comparison with the non-padded reconstruction (Figure 2b) suggests that zero-padding the experimental data results in a significant improvement in the reconstruction quality.

To quantitatively assess the quality of the reconstructed phase images we have evaluated both resolution and contrast. To measure the resolution of the phase reconstruction we consider the highest frequency peak visible in the power spectrum and the average full width half maximum (FWHM) of the intensity at atomic sites. We define contrast as the reduction in intensity between the Mo and 2S atomic sites as a fraction of the 2S atomic site intensity.

Inspection of the power spectrum calculated from the zero-padded phase image (Figure 3d) shows weak information at 1.58Å which is not present in the power spectrum of the non-padded phase reconstruction (Figure 3g). Gaussian fits to the line scans shown in Figure 3e and h give values for mean FWHM of 3.7±1Å for the non-padded reconstruction and 2.0±0.3Å for the zero padded reconstruction (see Supplementary Figure S4), with uncertainties calculated from the standard deviation of the width of the four Gaussian functions used in the fits. This apparent increase in information is discussed later. The contrast of the non-padded phase reconstruction (Figure 3h) is approximately 0.04 whereas the zero-padded phase reconstruction (Figure 3e) has contrast of 0.14.

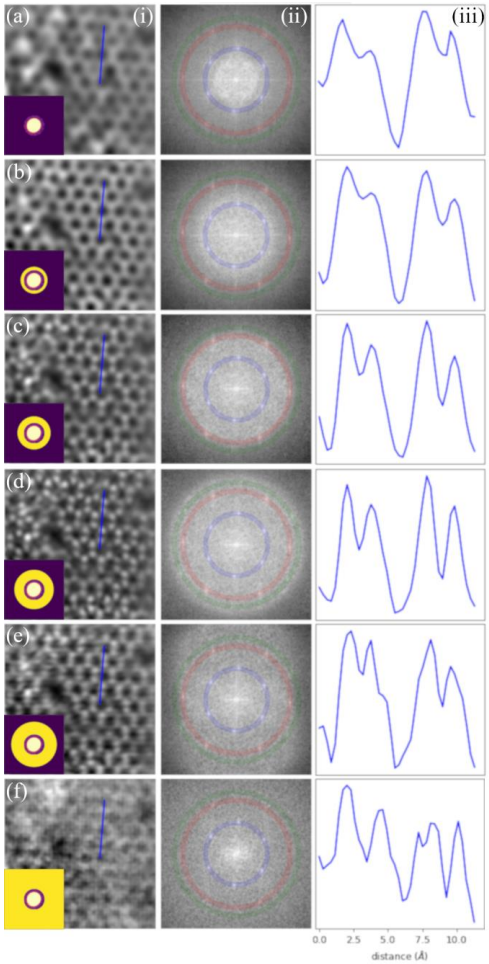

Figure 4. Column (i) reconstructed object phase (inset shows the PACBED pattern with yellow annular region corresponding to the applied annular mask), (ii) power spectrum of and (iii) intensity line scans through the phase. Yellow regions in the PACBED images represent the angular range in diffraction space allowed to float in the ePIE reconstruction. Angular ranges are (a) 0mrad, (b) 13mrad, (c) 26mrad, (d) 39mrad , (e) 52mrad and (f) 82mrad.

Allowing ePIE to fill in information at scattering angles higher than those measured on the detector can be achieved by applying an annular mask to the zero-padded data as shown in Figure 4 b) – f)

column i). The regions marked in yellow in figure 4 are not constrained by the measured diffraction pattern, the algorithm updates them at each iteration with values from the forward model calculated from the probe and object function. This approach has been demonstrated optically by Maiden and colleagues to recover diffraction information beyond that used in the update procedure. [35] The reconstructed probe functions and root mean square error for the reconstructions is shown in supplementary information Figures S5 and S6.

The angular range of the masked extended region is increased in fractions of the convergence semi-angle from 0.5α up to 2α beyond the maximum measured scattering angle (in steps of 0.5α). Finally, the entire zero-padded region is allowed to float corresponding to an extended region of 82mrad, greater the 3α. The images in Figure 4 have been smoothed with a gaussian kernel with a standard deviation of 1 pixel to remove high frequency noise. Reconstructions prior to gaussian filtering can be found in Supplementary Figure S7. The effect on the contrast and resolution of the reconstructed phase is shown in Figure 4 and measurements of contrast and resolution are given in Table I. To quantify resolution in the object reconstruction multiple metrics are considered using both fits to the atomic positions in real space and measurements from the calculated 2D power spectrum. Details can be found in Supplementary Information Figures S8 and S9 as well as Table S1.

Table I. Contrast and resolution measurements.

Extended region		Contrast	Resolution		
Factor of α	mrad		Reflection (Å)	FRC 0.5 bit (Å)	1D fit mean FWHM (Å)
0	0	0.14	2.73	2.34	2.0±0.3
0.5	13	0.15	1.58	1.42	1.7±0.1
1	26	0.38	1.58	1.31	1.3±0.1
1.5	39	0.55	1.36	1.31	1.2±0.1
2	52	0.34	1.58	1.47	1.4±0.1
>3	82	0.35	2.73	n/a	1.4±0.3

As the angular range of the extended region is increased up to a width of 1.5 times the convergence semi angle both the resolution and the contrast of the reconstruction improves. Beyond 1.5α there is a deterioration in the quality of the reconstruction. The maximum resolution as measured from the mean FWHM of the atomic positions is 1.2 ± 0.1Å with a measured contrast of 0.55, an increase of 1.7 times in resolution and in contrast by a factor of 4. The Abbe limited resolution of an optical system is approximately equivalent to the FWHM of the point spread function and by this definition we achieve a resolution of 1.2 ± 0.1Å equivalent to the position averaged TEM images from a Cs and Cc corrected TEM [4]. Two dimensional Gaussian fits to all atoms in the reconstructed image suggest that the true Abbe resolution may be slightly better than this (see Supplementary Information Figure S8 and Table S1). A Fourier ring correlation (FRC)

measurement gives a 0.5 bit resolution of 1.31 Å for both 26 and 39 mrad extended regions (see Supplementary Information figure S9). [36].

The recovery of information at scattering vectors higher than those measured in the experiment can be seen in the PACBED patterns for each reconstruction (Supplementary Figure S9), clearly showing diffraction information beyond the limits of the detector. The physical explanation of this is as follows. The incident illuminating electrons have a dispersion of momentum vectors and in reciprocal space the incident beam is a disc with a radius equal the convergence semi-angle. Scattering from the sample to a particular frequency, for example a specific crystallographic Bragg reflection, will also have the same dispersion of momentum vectors: consequently, the Bragg spot is broadened to a disc with radius equal to that of the BFD. If a reflection lies outside the detector but some proportion of the convolution of the Bragg spot with the BFD lies within the detector then information at a specific spatial frequency is recorded in the CBED pattern and can, in principle, be recovered. For illustration, in Figure 5 information from the 1.58Å and 1.36Å reflections are encoded in the measured diffraction pattern whereas information from the 1.03Å reflection is unrecoverable. It can be argued that to correctly model the forward diffraction pattern in the iterative reconstruction scattering angles outside those recorded, but which interfere with pixels on the detector must be included for quantitative reconstruction.

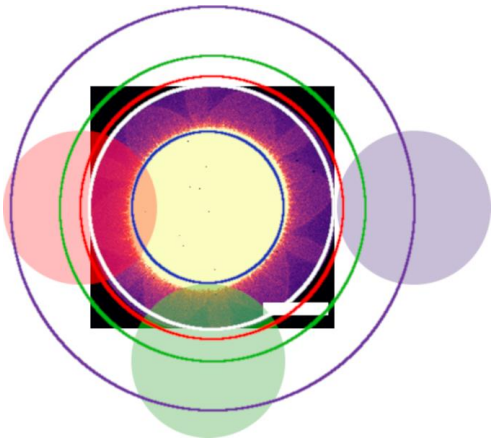

Figure 5. PACBED pattern from monolayer MoS_2 overlayed with the positions of the first four reflections at 2.73Å (blue circle), 1.58Å (red circle), 1.36Å (green circle) and 1.03Å (purple circle). The white circle at 1.7Å marks the inner angle of the ADF detector. The Bragg discs at 1.58Å (filled red circle) and 1.36Å (filled green circle) overlap the detector and information at these length-scales can be recovered. The Bragg disc at 1.03Å does not overlap with the detector and no information can be recovered.

The improvement in image quality seen in the zero-padded compared to the raw data reconstructions (Figure 3c and f) is due to the ability of the ptychographic model to include higher frequencies in the forward model of the complex diffraction pattern. In the zero padded data these

are forced to zero prior to the reverse propagation deconvolution into probe and object functions limiting the resolution in the reconstruction for this example to no greater than the 1.7Å detector aperture limit but with a relaxed Nyquist sampling condition.

The highest quality reconstruction was recovered for an extended region at 1.5α (Table 1 and Figure 4). This appears to be contrary to the argument that the maximum angle beyond the detector limit which is recoverable is equal to the convergence semi-angle α. We attribute this to two factors: Firstly, a slight mis-centring of the BFD in the experimental diffraction patterns and secondly for an extended region of α, the highest reconstruction frequency is at the information Nyquist limit and in practice a small oversampling of the image enables better interpretability without the need for further interpolation. As it is not possible to recover information at angles greater than α beyond the detector limit, reconstructions with masked extended regions at angles higher than 1.5α show a deterioration in quality. Although for reconstructions with $> 1.5\alpha$ extended region the ptychographic algorithm appears to converge (see RMSE plots, supplementary figure S6) there is both a significant addition of high frequency noise to the object function, and high frequency features in the reconstructed probe indicative of poor deconvolution of the probe and object functions (Table 1, Figure 4 and Supplementary Figures S5 and S7). The PACBED patterns for these high extended region reconstructions show clear Fourier repeats at high frequencies indicating a failure of the algorithm to correctly converge (Supplementary Figure S10).

We have shown that allowing regions beyond the detector to float enables electron ptychography to populate spatial frequencies not directly measured and enhances the quality of the reconstruction. The limitations on the detector super-resolution are set by the convergence semi-angle with the maximum recoverable scattering vector being the sum of the detector and the convergence semi-angles. Above this limit the extrapolation of information is unreliable. In this instance we have utilised this to enable simultaneous collection of ptychographic and MAADF images from mono-layer MoS_2. We have also demonstrated an increase in resolution at 30keV beyond that obtained using standard probe-based imaging techniques using a non-monochromated, third-order aberration corrected cold-FEG STEM.

Supplementary Material

See supplementary material for details of the reconstructed probe functions, RMSE error plots, details of the calculation of resolution and reconstructed PACBED patterns.

Acknowledgements

The authors thank Dr. Frederick Allars for helpful conversations. We thank Diamond Light Source for access and support in use of the electron Physical Science Imaging Centre (Instrument E02 proposal number EM19493) that contributed to the results presented here.

References

[1] S. J. Pennycook and P. D. Nellist, editors , Scanning Transmission Electron Microscopy (Springer New York, New York, NY, 2011).

[2] B. Fultz and J. Howe, Transmission Electron Microscopy and Diffractometry of Materials (Springer Berlin Heidelberg, Berlin, Heidelberg, 2013).

[3] R. F. Egerton, Mechanisms of Radiation Damage in Beam-Sensitive Specimens, for TEM Accelerating Voltages between 10 and 300 KV, Microsc. Res. Tech. 75, 1550 (2012).

[4] M. Linck, P. Hartel, S. Uhlemann, et al., Chromatic Aberration Correction for Atomic Resolution TEM Imaging from 20 to 80 KV, Phys. Rev. Lett. 117, 076101 (2016).

[5] H. Sawada, T. Sasaki, F. Hosokawa, and K. Suenaga, Atomic-Resolution STEM Imaging of Graphene at Low Voltage of 30 KV with Resolution Enhancement by Using Large Convergence Angle, Phys. Rev. Lett. 114, 166102 (2015).

[6] T. Sasaki, H. Sawada, F. Hosokawa, et al. Aberration-Corrected STEM/TEM Imaging at 15kV, Ultramicroscopy 145, 50 (2014).

[7] I. MacLaren, T. A. Macgregor, C. S. Allen, and A. I. Kirkland, Detectors—The Ongoing Revolution in Scanning Transmission Electron Microscopy and Why This Important to Material Characterization, APL Mater. 8, 110901 (2020).

[8] C. Ophus, Four-Dimensional Scanning Transmission Electron Microscopy (4D-STEM): From Scanning Nanodiffraction to Ptychography and Beyond, Microsc. Microanal. 25, 563 (2019).

[9] Z. Chen, Y. Jiang, Y.-T. Shao, et al. Electron Ptychography Achieves Atomic-Resolution Limits Set by Lattice Vibrations, Science (80-.). 372, 826 (2021).

[10] M. J. Humphry, B. Kraus, A. C. Hurst, et al. Ptychographic Electron Microscopy Using High-Angle Dark-Field Scattering for Sub-Nanometre Resolution Imaging, Nat. Commun. 3, 730 (2012).

[11] S. Cao, A. M. Maiden, and J. M. Rodenburg, Image Feature Delocalization in Defocused Probe Electron Ptychography, Ultramicroscopy 187, 71 (2018).

[12] J. Song, C. S. Allen, S. Gao, et al. Atomic Resolution Defocused Electron Ptychography at Low Dose with a Fast, Direct Electron Detector, Sci. Rep. 9, 3919 (2019).

[13] L. Zho, J. Song, J. S. Kim et al. Low-Dose Phase Retrieval of Biological Specimens Using Cryo-Electron Ptychography, Nat. Commun. 11, 2773 (2020).

[14] P. M. Pelz, W. X. Qiu, R. Bücker, et al. Low-Dose Cryo Electron Ptychography via Non-Convex Bayesian Optimization, Sci. Rep. 7, 9883 (2017).

[15] P. Wang, F. Zhang, S. Gao, et al. Electron Ptychographic Diffractive Imaging of Boron Atoms in LaB6 Crystals, Sci. Rep. 7, 2857 (2017).

[16] H. Yang, I. Maclaren, L. Jones, et al. Electron Ptychographic Phase Imaging of Light Elements in Crystalline Materials Using Wigner Distribution Deconvolution, Ultramicroscopy 180, 173 (2017).

[17] R. W. Gerchberg, Super-Resolution through Error Energy Reduction, Opt. Acta (Lond). 21, 709 (1974).

[18] A. M. Maiden, M. J. Humphry, F. Zhang, and J. M. Rodenburg, Superresolution Imaging via Ptychography, J. Opt. Soc. Am. A 28, 604 (2011).

[19] T. Sasaki, H. Sawada, F. Hosokawa, et al. Performance of Low-Voltage STEM/TEM with Delta Corrector and Cold Field Emission Gun, J. Electron Microsc. (Tokyo). 59, S7 (2010).

[20] S. de Graaf, M. Ahmadi, I. Lazić, et al. Real-Time Imaging of Atomic Electrostatic Potentials in 2D Materials with 30 KeV Electrons, Microsc. Microanal. 27, 1946 (2021).

[21] J. Rodenburg and A. Maiden, Ptychography, in Springer Handbook of Microscopy, edited by P. W. Hawkes and J. C. H. Spence (Springer, Cham, 2019), pp. 819–904.

[22] A. M. Maiden and J. M. Rodenburg, An Improved Ptychographical Phase Retrieval Algorithm for Diffractive Imaging, Ultramicroscopy 109, 1256 (2009).

[23] T. J. Pennycook, A. R. Lupini, H. Yang, et al. Efficient Phase Contrast Imaging in STEM Using a Pixelated Detector. Part 1: Experimental Demonstration at Atomic Resolution, Ultramicroscopy 151, 160 (2015).

[24] C. M. O'Leary, C. S. Allen, C. Huang, et al. Phase Reconstruction Using Fast Binary 4D STEM Data, Appl. Phys. Lett. 116, 124101 (2020).

[25] J. A. Mir, R. Clough, R. MacInnes, et al. Characterisation of the Medipix3 Detector for 60 and 80 KeV Electrons, Ultramicroscopy 182, 44 (2017).

[26] G. Moldovan, I. Sikharulidze, J. Matheson, et al. Characterisation of a Counting Imaging Detector for Electron Detection in the Energy Range 10-20 KeV, Nucl. Instruments Methods Phys. Res. Sect. A Accel. Spectrometers, Detect. Assoc. Equip. 681, 21 (2012).

[27] P. D. Nellist, Scanning Transmission Electron Microscopy, in Springer Handbook of Microscopy, edited by P. W. Hawkes and J. C. H. Spence (Springer, Cham, 2019), pp. 49–99.

[28] P. D. Nellist and J. M. Rodenburg, Beyond the Conventional Information Limit: The Relevant Coherence Function, Ultramicroscopy 54, 61 (1994).

[29] D. J. Batey, D. Claus, and J. M. Rodenburg, Information Multiplexing in Ptychography, Ultramicroscopy 138, 13 (2014).

[30] Y. Yao, T. Jiang, J. Klug et al. Broadband X-Ray Ptychography Using Multi-Wavelength Algorithm, J. Synchrotron Radiat. 28, 309 (2021).

[31] D. J. Batey, Ptychographic Imaging Of Mixed States, University of Sheffield, 2014.

[32] A. M. Maiden, M. J. Humphry, M. C. Sarahan, et al. An Annealing Algorithm to Correct Positioning Errors in Ptychography, Ultramicroscopy 120, 64 (2012).

[33] P. Thibault and A. Menzel, Reconstructing State Mixtures from Diffraction Measurements, Nature 494, 68 (2013).

[34] S. Cao, P. Kok, P. Li, et al. Modal Decomposition of a Propagating Matter Wave via Electron Ptychography, Phys. Rev. A 94, 063621 (2016).

[35] A. M. Maiden, M. J. Humphry, F. Zhang, and J. M. Rodenburg, Superresolution Imaging via Ptychography, J. Opt. Soc. Am. A 28, 604 (2011).

[36] M. Van Heel and M. Schatz, Fourier Shell Correlation Threshold Criteria, J. Struct. Biol. 151, 250 (2005).

PLEASE CITE THIS ARTICLE AS DOI: 10.1063/5.0143684

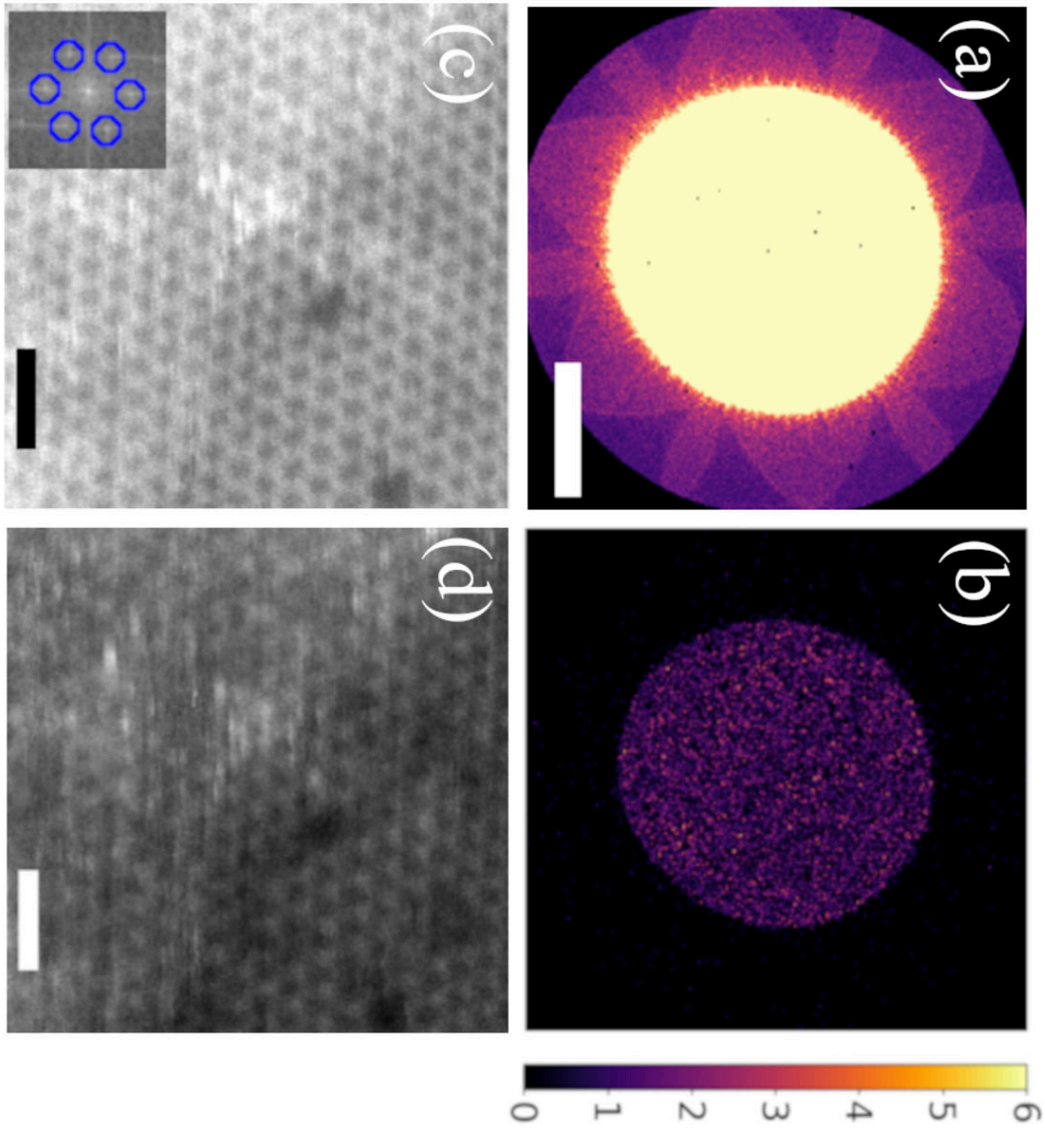

Applied Physics Letters

PLEASE CITE THIS ARTICLE AS DOI: 10.1063/5.0143684

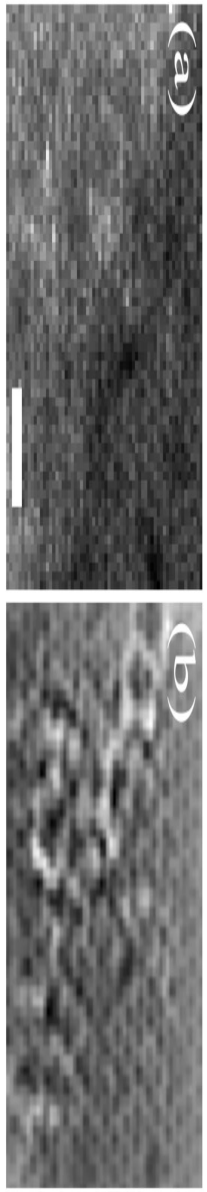

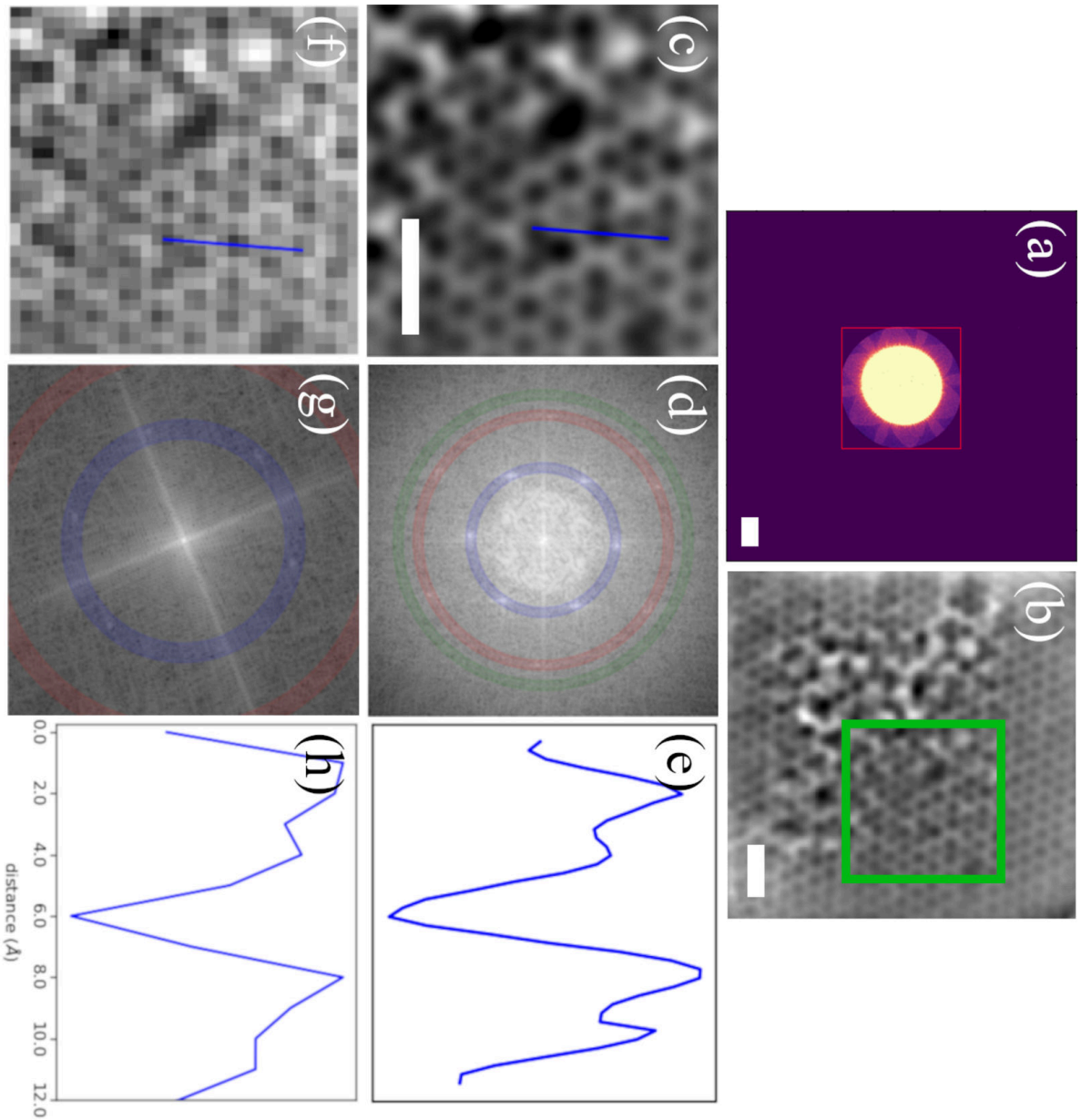

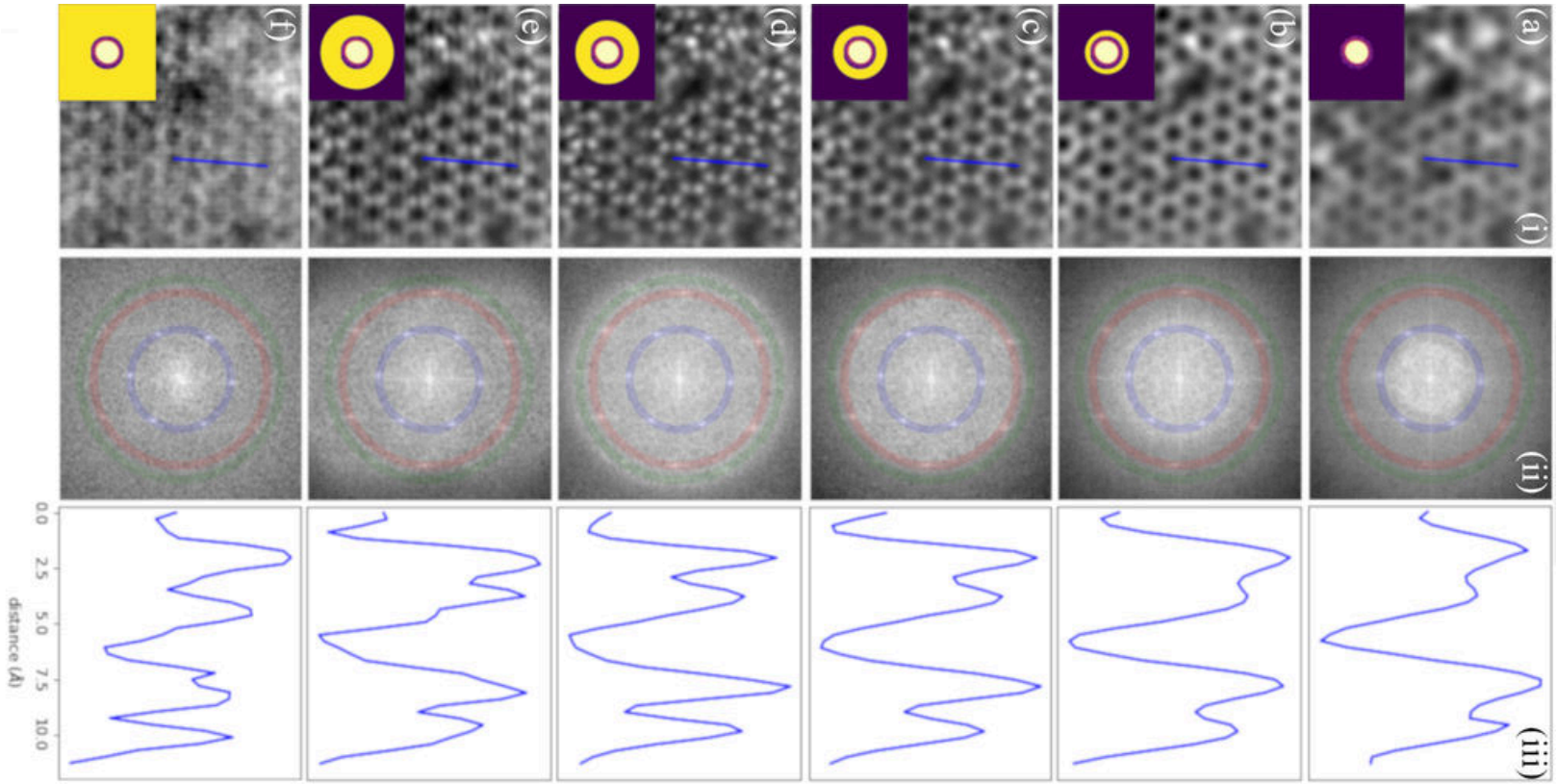

Applied Physics Letters

PLEASE CITE THIS ARTICLE AS DOI: 10.1063/5.0143684